Research Paper

Data-driven modeling for evaluating deformation of a deep excavation near existing tunnels

Fengwen Lai [a], Songyu Liu [b], Jim Shiau [c], Mingpeng Liu [d,*], Guojun Cai [e], Ming Huang [a]

[a] *College of Civil Engineering, Fuzhou University, Fuzhou 350108, China*
[b] *Institute of Geotechnical Engineering, Southeast University, Nanjing 211189, China*
[c] *School of Engineering, University of Southern Queensland, Toowoomba 4350, Australia*
[d] *Faculty of Civil Engineering, RWTH Aachen University, Aachen 52074, Germany*
[e] *School of Civil Engineering, Anhui Jianzhu University, Hefei 230601, China*

Abstract

This study explores an integrated framework combining in-situ test-based numerical and data-driven modeling to assess the performance of a deep excavation-tunnel system. To achieve the goal, a case history of deep excavations adjacent to existing tunnels in silt/sand-dominated sediments is introduced to establish a base three-dimensional finite element (3D-FE) model. In-situ tests such as cone penetration test (CPT/CPTU) and seismic dilatometer test (DMT/SDMT), as an alternative to laboratory testing, are used to determine a set of advanced constitutive model parameters. The established excavation-tunnel numerical model is then validated against filed monitoring data. A dataset from numerical simulation is created for training and testing four machine learning models (i.e., artificial neural network (ANN), support vector machines (SVM), random forest (RF), and light gradient boosting machine (LightGBM)), which predict the maximum wall deflection, ground surface settlement, horizontal and vertical displacements of the tunnel. Results show that the ANN model outperforms other models in prediction capacity. Its generalization ability in practice is further enhanced by comparing field measurement data and empirical equations. The findings suggest that, with the integrated in-situ tests, FE and ANN modeling could be used to predict deformation responses of deep excavations close to existing tunnels in soft soil. The present study is useful and valuable for practical risk assessment and mitigation decisions.

Keywords: Numerical modeling; Data-driven modeling; In-situ test; Deep excavation; Tunnel; Soft soil; Deformation response

1 Introduction

Rapid urban development in densely populated areas has led to an increasing need for the construction of deep excavations and tunnels. As more tunnels have been constructed to alleviate traffic congestion, deep excavations are inevitably performed close to these existing tunnels to facilitate infrastructure systems (Doležalová, 2001; Hu et al., 2003; Huang et al., 2013). Consequently, the construction of deep excavations unavoidably would cause ground movements, which may, in turn, affect the serviceability of nearby tunnel linings (e.g., crack and leakage) (Chen et al., 2016; Meng et al., 2021). It is a critical design concern to quantitatively determine what magnitude of deformation is generated in deep excavations and nearby tunnels, and hence to achieve safe and efficient construction as well as prevention of damage to existing tunnels.

Observational, experimental, analytical, and numerical approaches have all been extensively used to evaluate the performance of deep excavations adjacent to existing tunnels (Meng et al., 2022, 2025; Wei et al., 2025; Xu et al., 2025). Field observational approach is always an attractive solution to gain insight into the responses of existing tunnels to deep excavations (Lai et al., 2022; Liu et al., 2020;

---

* Corresponding author.
  E-mail address: mingpeng.liu@rwth-aachen.de (M. Liu).
Peer review under the responsibility of Tongji University

Meng et al., 2020). A critical prerequisite for its successful implementation is real-time feedback of information provided from the monitoring data. Therefore, it is generally a resource-demanding and lengthy process (Lai et al., 2021). The limited testing data also hinder a thorough and accurate evaluation of the responses. Analytical solutions have been also proposed to estimate deformations of deep excavations and nearby existing tunnels (Cheng et al., 2020; Liang et al., 2018; Lu et al., 2023a; Zhang et al., 2013). Among these, the two-stage method is of representativeness. However, formulating the soil-structure interaction is highly difficult, even though very complicated equations have been derived in previous analytical solutions. In addition, complicated equations may not be favored in practical applications.

Numerical modeling that allows complex soil-structure interaction, soil constitutive models, interfaces, and required boundary conditions, particularly in finite element (FE), has been recognized as a powerful tool to study the deep excavation-soil-tunnel interaction and hence to estimate deformations induced by deep excavations and nearby tunnels (Chen et al., 2016; Li et al., 2018, 2019; Lu et al., 2023b; Shi et al., 2015; Zhuang et al., 2023). However, the accuracy of numerical results highly relies on the selection of constitutive models, of which the model calibration of empirical parameters is a challenging step for their practical application (Liu et al., 2024c).

The constitutive model calibration is generally done by laboratory testing, while gaining available testing data requires a certain number of high-quality samples and rigorous testing procedures. However, for coarse-grained and silt-dominated soils, it is a very difficult task to obtain "undisturbed" samples for laboratory testing. To overcome this difficulty, one possible alternative is to rely on in-situ tests as discussed by several researchers (Di Mariano et al., 2019; Fabris et al., 2021; Lai et al., 2025; Marzouk et al., 2024; Schmüdderich et al., 2020; Van Berkom et al., 2022). By integrating two widely used in-situ testing methods, it is feasible to calibrate an advanced soil constitutive model, i.e., strength-dominated piezocone penetration test (CPTU) and stiffness-dominated seismic dilatometer test (SDMT).

Despite its widespread use, numerical modeling remains a time-consuming approach for estimating deformation responses induced by deep excavations and nearby tunnels, primarily due to the challenges of soil constitutive model calibration. Therefore, a simpler and more efficient alternative has long been sought. Recent advances in machine learning (ML) present a promising solution through data-driven surrogate models that combine physics-based simulations with big data analytics (Guo et al., 2023; Lai et al., 2023; Mishra et al., 2024; Samaniego et al., 2020; Singh & Budarapu, 2024; Siruvuri et al., 2023; Varma Siruvuri et al., 2022; Zhuang et al., 2021). Unlike traditional numerical methods, which rely on rigorous physical formulations and manual parameter calibration, these ML-based approaches leverage big dataset to directly address complex nonlinear problems.

By automating feature extraction from available data, they significantly streamline the prediction process (Liu et al., 2024b). For a deep excavation and nearby tunnels, it allows forecasts of deformation responses based on the current excavation stage, so as to decide whether additional countermeasures to protect the existing tunnels during construction are needed. For this purpose, a key focus of this paper is to integrate in-situ test-based numerical and data-driven modeling for forecasting the maximum wall deflections, surface ground settlements, and tunnel displacements in a deep excavation-soil-tunnel system.

The present work is organized as follows. A three-dimensional (3D) FE model is first established based on a case history of a deep excavation adjacent to two existing tunnels, where the soil is modeled using an advanced double hardening plasticity model, i.e., hardening soil model with small strain stiffness (HSSmall) model (Benz, 2007; Schanz et al., 1999). A calibration approach for a set of the HSSmall model parameters based on CPTU/SDMT is then developed. The FE model established is further validated against measurement data to serve as a benchmark model toward the generation of a numerical dataset to construct data-driven models capturing the maximum deformation responses of a deep excavation-soil-tunnel system. On this basis, four widely used machine learning algorithms are used to train and test such a dataset. Their performance is validated and further compared to each other to find the optimal model, of which the generalization in practical application is finally discussed against the field monitoring data and previous empirical equations.

2 Overview of the project

2.1 Project description

A deep excavation project adjacent to two existing tunnels, denoted as up-track tunnel (UT) and down-track tunnel (DT) in Suzhou, Southeast China, was selected as a case study (Fig. 1). UT was located 12 m from the excavation site (outside diaphragm walls). The passive zone was reinforced with 6.0 m-wide, 23.6 m-deep mixing columns (DMC). Both tunnels had 6.2 m outer diameters, 11.9 m buried depths, and 0.35 m thick segmental linings, with a 6.3 m center-to-center spacing. As shown in Fig. 2, the excavation was proceeded in five steps to levels of 2.0, 6.5, 10.8, 14.8, and 18.5 m below ground level (BGL), denoted as Stages 1–5. The support system is composed of a diaphragm wall with an embedded depth of 50.5 m and four levels of concrete struts at 1.0, 5.5, 9.8, and 13.8 m BGL. Prior to performing each excavation step, the groundwater table was lowered to 1.0 m below the excavation level.

2.2 Geotechnical conditions

The excavation site was situated in the Taihu Lake Delta. Cone/piezocone penetration tests (CPT1–CPT3
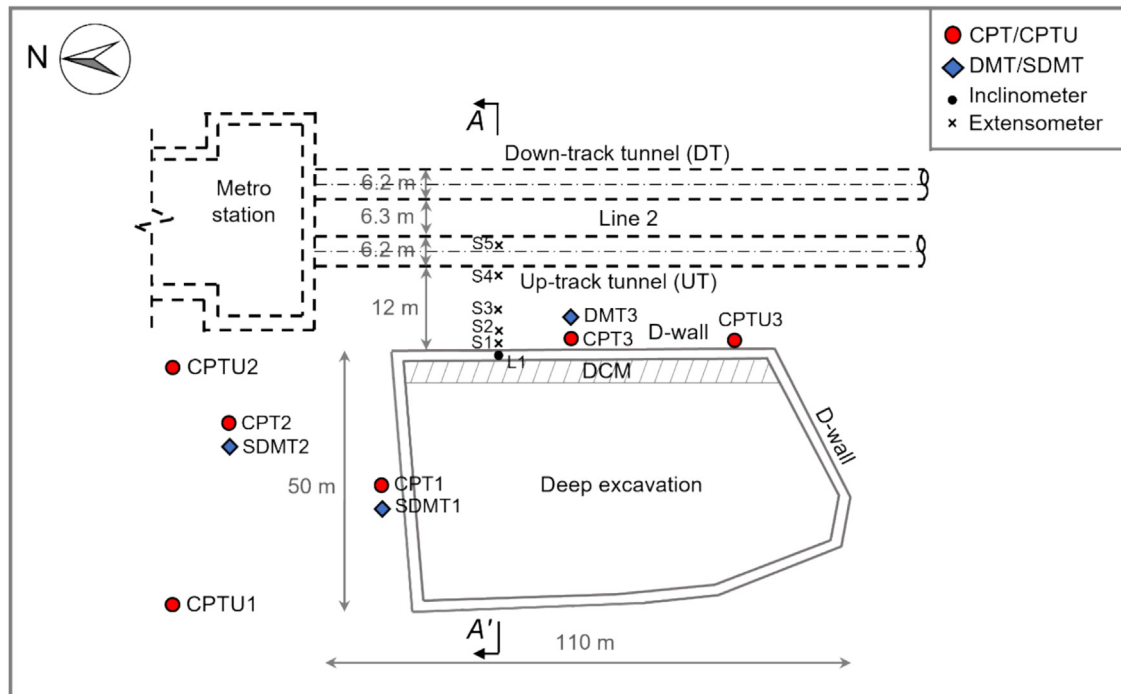
Fig. 1. Plan view of the project and layout of in-situ tests (Suzhou, Southeast China).

and CPTU1–CPTU2) were carried out to characterize soil layering (Fig. 3). During CPT/CPTU testing, a 15 cm^2 cone with a 60° tip was hydraulically pushed into ground at 2.0 cm/s using 1 m long penetration rods. The soil classification was achieved using the system of CPT-based soil behavior type (SBT), updated by Robertson (2016), revealing the following stratigraphy with a groundwater table at approximately 2.5 m BGL:

- Surface layer (0–3.8 m BGL): made ground (MG);
- Upper strata (3.8–21.1 m BGL): intermittent layers of medium-dense silty sand with sandy silt (GU1, 3.8–13.9 m BGL), firm to hard silty clay (GU2, 13.9–17.4 m), and medium-dense sandy silt with silty clay (GU3, 17.4–21.1 m);
- Intermediate layer: silty clay (GU4, 21.1–30.5 m BGL);
- Lower strata: thick layers of well-graded, medium-dense sandy silt with silty clay (GU5, 30.5–47.1 m BGL) and firm, organic silty clay with low plasticity and high compressibility (GU6, 47.1–100.0 m).

The soil stratification presents significant challenges for obtaining intact samples from boreholes due to the high content of fine silt and sand particles. These conditions make advanced laboratory element testing for soil constitutive model calibration particularly difficult. Consequently, in-situ testing was prioritized as a more practical alternative. Additional SDMTs and general dilatometer tests (DMTs) were conducted at the site (Fig. 1). The DMT/SDMT system incorporated two geophones spaced 50 cm apart vertically, mounted between the penetration rods and the flat dilatometer blade. Figure 4 shows the resulting

profiles: dilatometer modulus (E_D), horizontal stress index (K_D), material index (I_D), and shear wave velocity (V_s). Details on how to determine soil constitutive model parameters will be discussed in a later section.

2.3 Instrumentation

The representative section A-A' was instrumented with different sensors before excavations, as shown in Fig. 2. The plan view of instrumentation points can be found in Fig. 1. These include (a) five extensometers (S1–S5) to monitor the surface ground settlement, (b) one inclinometer tube (L1) to monitor the profile of wall deflections, and (c) five displacement markers (T1–T5; see Fig. 2) to document tunnel convergence induced by deep excavations. The readings started before the soil excavations (after the installation of diaphragm walls), and the comparison between numerical results and monitoring data are mainly for the period of soil excavation (Stages 1–5). It is reasonable to assume that the deformation responses before the soil excavation in the numerical model are set as zero. This would be consistent with field measurements.

3 In-situ test-based numerical modeling

3.1 Establishment of numerical model

Numerical studies were conducted throughout the paper using the FE program PLAXIS 3D (Brinkgreve et al., 2016). Figure 5 shows a base numerical model and its mesh. The soil domain was discretized into 360 000 10-
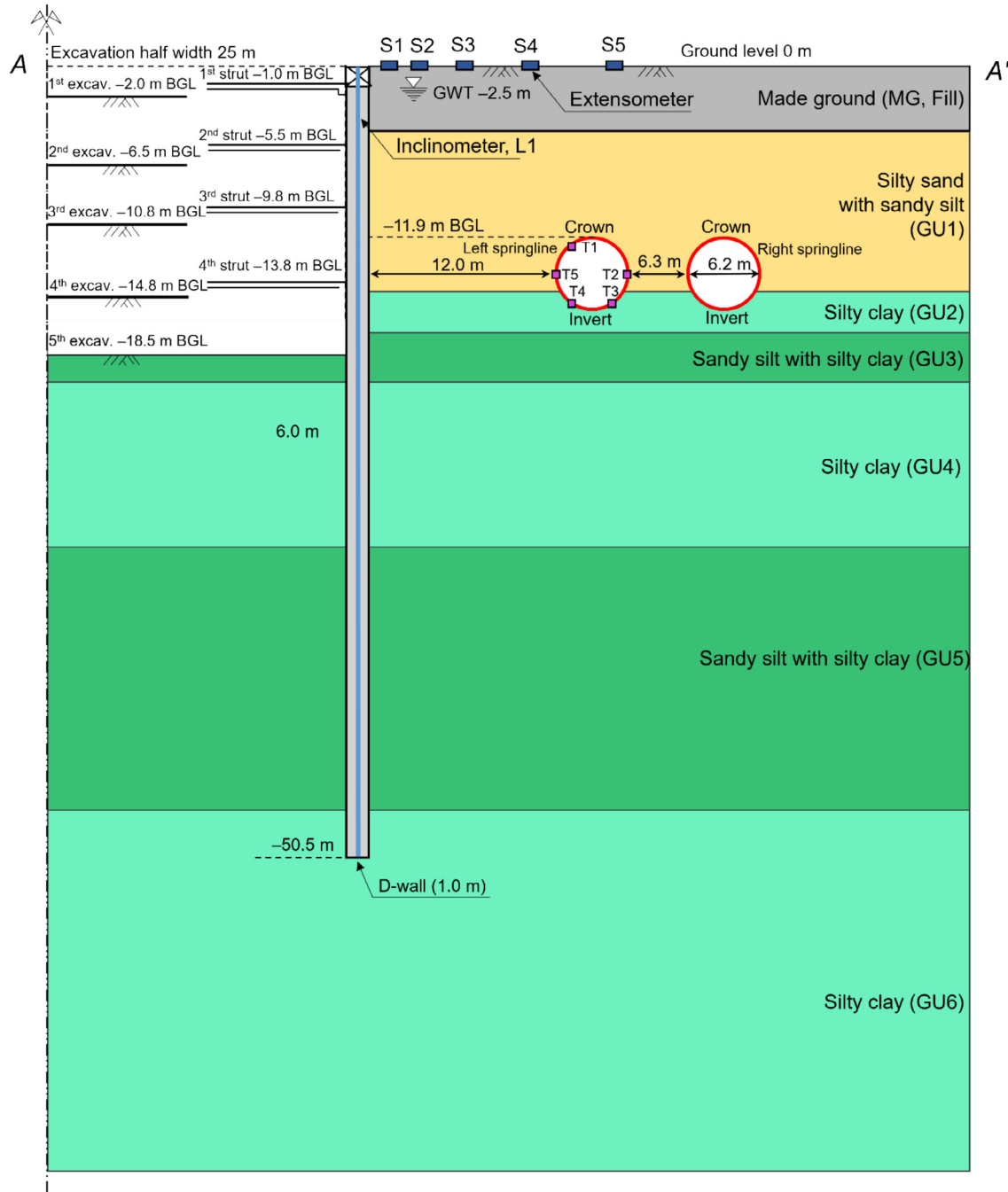
Fig. 2. Cross section of *A-A'* with soil layering.

noded tetrahedral elements, the diaphragm walls and tunnel linings were both simulated using plate elements, and the horizontal struts were considered as node-to-node anchor elements. The interface elements were imposed to take soil-structure interaction into account for diaphragm walls and tunnels. The computational domain was set as 350 m × 350 m × 100 m so that the influence of boundary effects could be avoided. Only vertical displacement is allowed for lateral (roller) boundaries, and full fixity (pin) is assigned to the bottom of the model.

The diaphragm walls, tunnel lining, and strut were considered as elastic materials with a Poisson's ratio of $v = 0.2$. The diaphragm wall had a Young's modulus (E) of 27.81 GPa, determined using $3290\sqrt{f_c}$ (ACI Committee, 2008; Ou, 2006), which considers the effects of cracks and defects within concrete. Standard compressive strength of concrete f_c was 35 MPa in this study. The Young's modules of 30.0 and 24.2 GPa were respectively adopted for the horizontal struts and tunnel linings. For diaphragm wall and tunnel linings, a strength reduction coefficient in the inter-
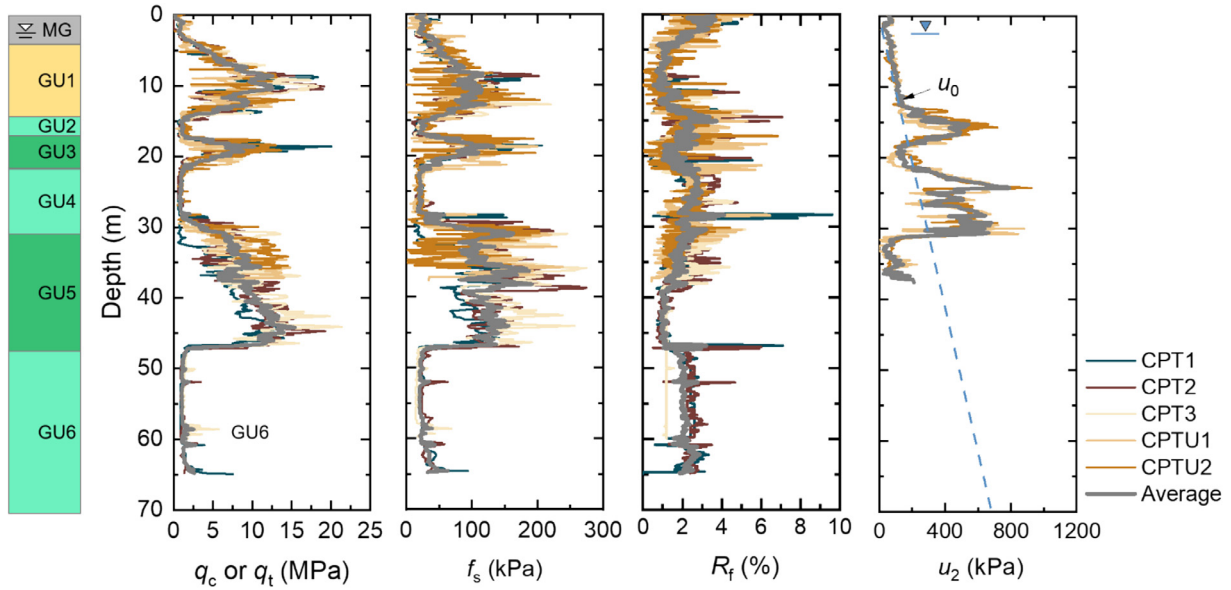
Fig. 3. Profiles of cone/piezocone penetration tests (CPT/CPTU). (Note: q_c or q_t denotes cone resistance; f_s denotes side friction; R_f is the ratio of q_c to f_s; u_2 denotes pore water pressure; u_0 denotes static water pressure.).
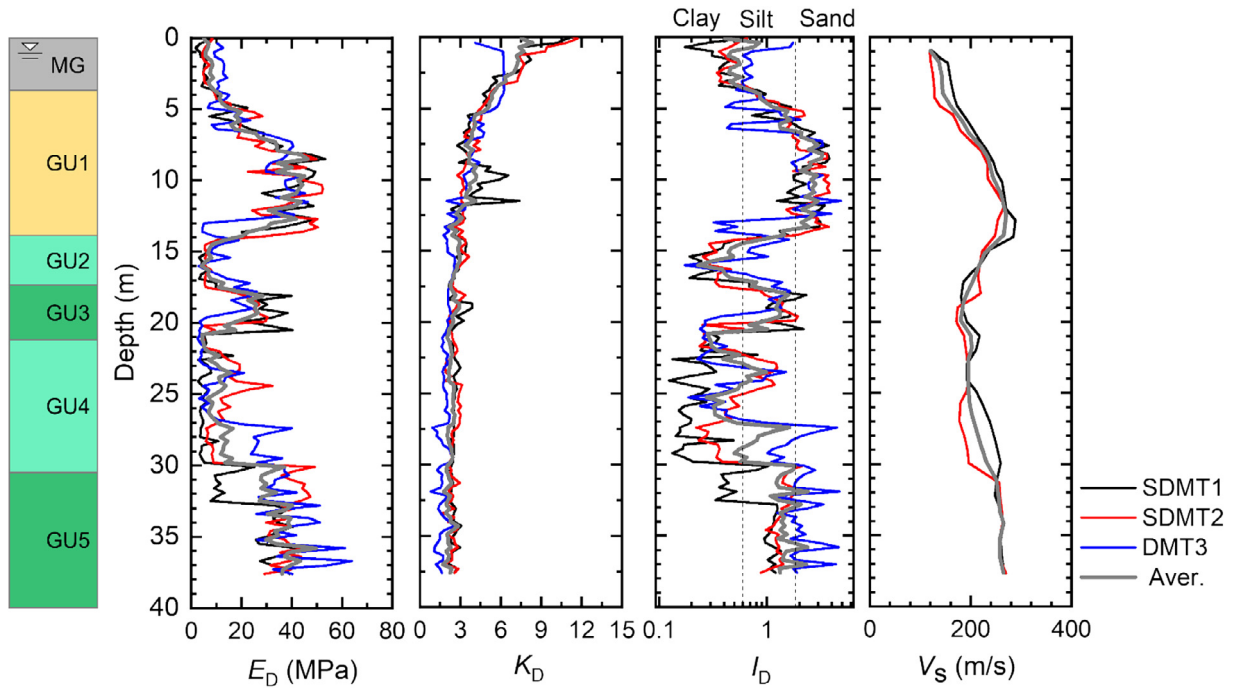

Fig. 4. Profiles of seismic and regular dilatometer tests.

face of $R_{inter} = 0.67$ (Daxer et al., 2023; Khoiri & Ou, 2013; Lai et al., 2021; Schweiger, 2014) was chosen to represent the soil-structure interaction.

3.2 Soil constitutive model and parameter estimation

The stress-dependent nature of soil stiffness should be properly accounted for in excavation-induced deformation analysis. During wall installation and subsequent excavation, soils experience varying strain levels, leading to shear modulus degradation. To address these effects, we selected the HSSmall model for the varying soil layers (Fig. 2).

As discussed before, the subsurface soil strata consisted of both fine-grained and coarse-grained materials, for which the HSSmall model parameters need to be calibrated separately. This study presents a unified approach for determining HSSmall model parameters using in-situ test-based empirical correlations (Table 1).

Key soil parameters, including effective friction angle (φ'), dilation angle (ψ'), unit weight (γ_{sat}), overconsolidation
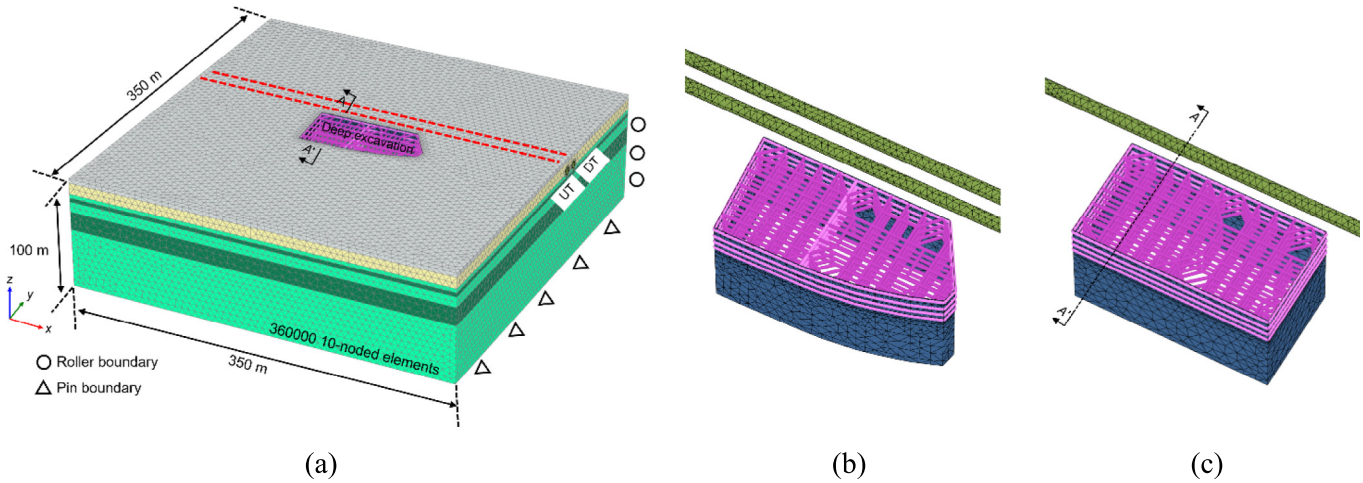
Fig. 5. 3D-FE models. (a) Mesh, (b) structure elements used for validation, and (c) structure elements used for the development of big data.

ratio (OCR), and permeability (k) can be directly estimated based on CPT/CPTU data, where merely the CPTU data are used for the determination of φ' of fine-grained soils. The oedometric stiffness (E_{oed}^{ref}) can be obtained from DMT/SDMT data, while small strain stiffness (G_0^{ref}) is calculated by SDMT-measured shear wave velocity. The other parameters are estimated by simplified correlations/assumptions. For example, the earth pressure coefficient at rest (K_0) is calculated using a previous correlation. Effective soil cohesion (c') is estimated using effective overburden stress for over-consolidated fine-grained soil. The parameter m is determined considering soil density and stiffness, ranging from 0.5 to 1.0. Both E_{50}^{ref} and E_{ur}^{ref} can be estimated from E_{oed}^{ref}, depending on various soil types, as detailed in Table 1. Shear strain at $70\% G_0^{ref}$ ($\gamma_{0.7}$) was determined by plotting a curve of normalized shear modulus (G/G_0) against shear strain (γ_s). Based on the in-situ testing results, Table 2 presents a full set of HSSmall model parameters for various soil layers based on in-situ test results.

3.3 Model comparison and validation

Figures 6 and 7 present the comparison in terms of deformation responses (wall deflections, ground surface settlements, and tunnel lining displacements) obtained from in-situ test-based numerical model and field monitoring data from Section *A-A'* (Figs. 1 and 2). The predicted wall deflections and ground settlements show excellent agreement with monitoring data, while minor discrepancies in wall movements may be attributed to a slight overestimation of Young's modulus in the linear elastic model (Fig. 6).

Similarly, Fig. 7 indicates that computed tunnel lining displacements align closely with the measured data, where soil heave during excavation caused greater movement at the left spring line than the right. The comparison comprehensively confirms that the in-situ test-based numerical model reasonably captures the deformation response

induced by deep excavations near existing tunnels, providing a tool to produce a robust dataset.

4 Development of an artificial dataset

4.1 Determination of influential factors

To generate an artificial dataset using the in-situ test-based numerical model, we first identify key input variables that significantly influence deformation responses. It has been demonstrated that excavation width (B) and excavation depth (H), soil undrained shear strength (s_u), and unloading/reloading stiffness (E_{ur}) have a pronounced impact on wall deflection. Since the normally consolidated (NC) soil is considered in this study, soil strength is characterized in terms of effective stresses, i.e., using effective friction angle (φ') and zero cohesion as the input. Additionally, E_{ur} is derived from the correlations with oedometric stiffness (E_{oed}) estimated by DMT. Therefore, two normalized parameters, $\tan\varphi'$ and E_{oed}/σ_v', are used to represent soil strength and stiffness properties. Kung et al. (2007) suggested that the stiffness of retaining structures should be considered to predict the maximum wall deflection, which is closely relevant to wall thickness (t). Tunnel displacements depend on its relative location to a deep excavation, quantified by horizontal distance (D_h) between wall and tunnel lining, and vertical tunnel crown depth (D_v).

Accordingly, the seven input variables are considered to predict the deformation responses of deep excavations and their nearby exiting tunnels. They can be categorized into four groups: (a) soil properties ($\tan\varphi'$ and E_{oed}/σ_v'), (b) deep excavation configuration (B and H), (c) wall thickness (t), and (d) relative tunnel location to deep excavation (D_h and D_v).

On the other hand, the output of the data-driven model includes four variables representing the deformation responses of deep excavations and nearby existing tunnels,

Table 1
Correlations used to estimate the HSSmall parameters through in-situ tests.

Category	Parameter	Correlation	Test type	Reference
Strength parameter	c' (kPa)	$c' = 0.03\sigma_{v0}'$, for OC fine-grained soil	–	Mayne (2016)
	φ' (°)	$\varphi' = 17.6 + 11.1\lg((q_c/p_a)(p_a/\sigma_{v0}')^{0.5})$, for coarse-grained soil	CPT/CPTU	Lunne et al. (2002)
		$\varphi' = 29.5\,B_q^{0.121}[0.256 + 0.336\,B_q + \lg Q]$ $B_q = (u_2 - u_0)/(q_t\text{-}\sigma_{v0})$ $Q = (q_t - \sigma_{v0})/\sigma_{v0}'$, for fine-grained soil	CPTU	Mayne (2007)
	ψ' (°)	$\psi' = 2.4\ln[\frac{q_c/p_a}{17.68(\sigma_{v0}'/p_a)^{0.5}}][12.1 - \ln(\frac{100q_c}{p_a})] - 0.9$	CPT	Lee et al. (2008)
State parameter	γ_{sat} (kN/m³)	$\gamma_{sat} = [0.27\lg R_f + 0.36\lg(q_t/p_a) + 1.236]\,\gamma_w$	CPT/CPTU	Robertson and Cabal (2010)
	K_0	$K_0 = (1 - \sin\phi') \times \text{OCR}^{\sin\phi'}$	CPT/CPTU	Mayne and Kulhawy (1982)
	OCR	$\text{OCR} = 0.32(q_t - \sigma_{v0})^{0.72}/\sigma_{v0}'$, for coarse-grained soil $\text{OCR} = 0.33(q_t - \sigma_{v0})/\sigma_{v0}'$, for fine-grained soil	CPT/CPTU	Mayne (2005); Agaiby and Mayne (2019)
Deformation parameter	E_{oed}^{ref} (MPa)	$E_{oed} = R_M E_D$ $R_M = 0.14 + 2.36\lg K_D$, for $(I_D \leq 0.6)$ $R_M = R_{M,0} + (2.5 - R_{M,0})\lg K_D$ $R_{M,0} = 0.14 + 0.15(I_D - 0.6)$, for $(0.6 < I_D < 3.0)$ $R_M = 0.5 + 2\lg K_D \geq 0.85$, for $(3 \leq I_D \leq 10)$ $R_M = 0.32 + 2.18\lg K_D \geq 0.85$, for $(K_D > 10)$	DMT/SDMT	Marchetti (1980)
	E_{50}^{ref} (MPa)	$E_{50}^{ref} = E_{oed}^{ref}$, for sand $E_{50}^{ref} = 1.25 E_{oed}^{ref}$, for silt/clay	DMT/SDMT	Schmüdderich et al. (2020)
	E_{ur}^{ref} (MPa)	$E_{ur}^{ref} = 3 E_{oed}^{ref}$, for medium to dense sand $E_{ur}^{ref} = 4 E_{oed}^{ref}$, for loose sand or silt $E_{ur}^{ref} = 5 E_{oed}^{ref}$, for clay	DMT/SDMT	Schmüdderich et al. (2020)
	m	0.5–1.0 for dense/stiff to loose/soft soil	–	Schmüdderich et al. (2020)
	G_0^{ref} (MPa)	$G_0 = \rho v_s^2$	SDMT	Amoroso et al. (2014)
	$\gamma_{0.7}$	$G/G_0 \sim \gamma_s$ curve: $\frac{G}{G_0} = \dfrac{1}{1 + \left(\frac{G}{G_{DMT}} - 1\right)\frac{\gamma_s}{\gamma_{DMT}}}$ $G_{DMT} = \frac{1-2v}{2(1-v)} M_{DMT}$ $\gamma_{DMT} = 0.3\%$, for sand $\gamma_{DMT} = 1.0\%$, for silt $\gamma_{DMT} = 1.5\%$, for clay	SDMT	Amoroso et al. (2014)
Permeability parameter	k (m/d)	$k = 10^{(0.952 - 3.04 I_c)}$, $1.0 < I_c \leq 3.27$ $k = 10^{(-4.52 - 1.37 I_c)}$, $3.27 < I_c < 4.0$ $I_c = [(3.47 - \lg Q_{t1})^2 + (\lg F_r + 1.22)^2]^{0.5}$ $Q_{t1} = (q_t - \sigma_{v0})/\sigma_{v0}'$ $F_s = f_s/(q_t\text{-}\sigma_{v0})$	CPT/CPTU	Robertson (2010)

Note: c' = effective cohesion; φ' = effective friction angle; ψ' = dilation angle; E_{50}^{ref} = primary loading stiffness (reference); E_{oed}^{ref} = oedometric stiffness (reference); E_{ur}^{ref} = un/reloading stiffness (reference); G_0^{ref} = small strain stiffness; $\gamma_{0.7}$ = shear strain at 70% G_0^{ref}; v_{ur} = un/reloading Poisson's ratio; m = stress dependency index; p^{ref} = reference stress; OCR = overconsolidation ratio; γ_{sat} = saturated unit weight; $K_{0,nc}$ = earth pressure coefficient for NC soil; K_0 = earth pressure coefficient at rest; R_{inter} = coefficient of soil strength reduction in interface element; k = permeability.

Table 2
HSSmall model parameters of different soil layers.

Soil layer		MG[a]	GU1	GU2	GU3	GU4	GU5	GU6[a]
Drainage condition		Undr.	Drained	Undr.	Undr.	Undr.	Undr.	Undr.
Top level (m)		0	3.80	13.90	17.40	21.10	30.50	47.10
Strength parameters	c' (kPa)	0	2.90	3.30	4.20	5.80	0	0
	φ' (°)	35.70	38.00	29.60	36.40	23.80	33.80	32.00
	ψ' (°)	1.00	5.90	0	5.20	0	5.10	0
Deformation parameters	E_{50}^{ref} (MPa)	4.30	44.27	10.69	19.92	8.52	20.29	16.60
	E_{oed}^{ref} (MPa)	4.30	44.27	8.55	15.93	6.81	16.23	8.30
	E_{ur}^{ref} (MPa)	12.90	132.81	42.74	63.73	34.06	81.15	49.80
	G_0^{ref} (MPa)	21.50	151.73	88.45	96.82	66.64	107.62	99.60
	$\gamma_{0.7}$	2.0×10^{-4}	1.4×10^{-4}	2.2×10^{-4}	3.2×10^{-4}	2.0×10^{-4}	3.1×10^{-4}	2.0×10^{-4}
	v_{ur}	0.20	0.20	0.20	0.20	0.20	0.20	0.20
	m	0.80	0.60	0.90	0.70	0.90	0.70	0.80
Other basic parameters	p^{ref} (kPa)	100.00	100.00	100.00	100.00	100.00	100.00	100.00
	OCR	1.00	1.86	3.68	1.15	1.87	1.00	1.00
	γ_{sat} (kN/m³)	17.10	19.00	17.50	19.10	17.40	19.80	18.30
	$K_{0,nc}$	0.42	0.38	0.51	0.41	0.60	0.44	0.47
	K_0	0.57	0.58	0.96	0.44	0.77	0.44	0.47
	R_{inter}	0.67	0.67	0.67	0.67	0.67	0.67	0.67
	k (m/d)	7.09×10^{-3}	4.19×10^{-1}	5.53×10^{-3}	2.28×10^{-2}	4.92×10^{-3}	1.75×10^{-2}	4.58×10^{-3}

[a]Deformation parameters from Liao et al. (2016);
$K_{0,nc}$ is the earth pressure coefficient for NC soil; and the definition of other parameters can refer to Table 1.
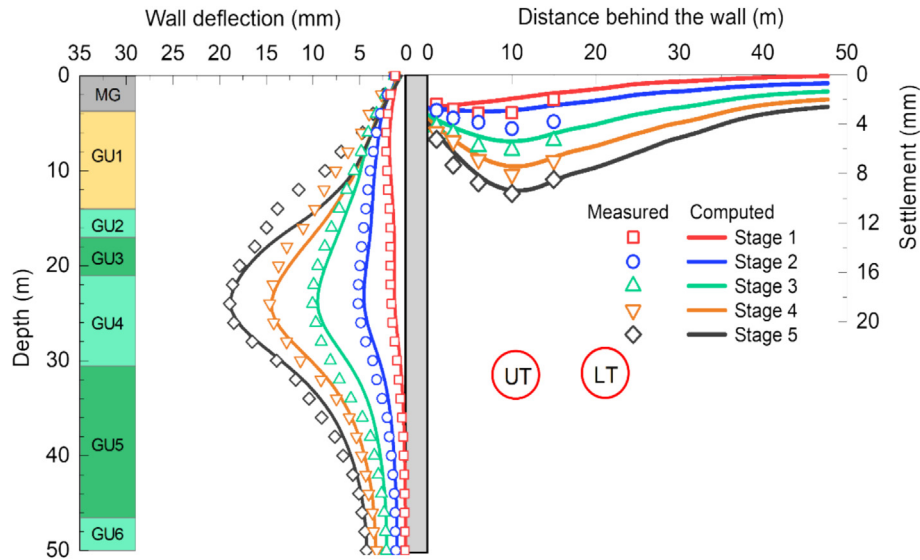

Fig. 6. Comparison of numerical results against field monitoring data for deep excavations.

namely the maximum horizontal and vertical tunnel displacement (Δ_{hm} and Δ_{vm}), the maximum wall deflection (δ_{hm}), and the maximum ground surface settlement (δ_{vm}), which can be directly extracted from the FE model.

4.2 Generation of artificial data using the FEM

A standard rectangular deep excavation adjacent to one existing tunnel in normally-consolidated homogeneous soil is postulated to simplify 3D-FE model, as shown in Fig. 5 (c), which is then used to develop an artificial dataset. The numerical results for the middle section of the deep excava-

tion and the nearby tunnel are utilized as the output (Fig. 5 (c)). Except for the last excavation step, horizontal support is imposed to maintain stability in each excavation step. The other details are kept the same with the established numerical model based on the case history. The soil properties are directly derived from in-situ tests. The variables of excavation size and wall thickness chosen in this study change below and above the data from the case history considered. The tunnel positions relative to deep excavations cover the various influential zones (Liu et al., 2024a). So the value ranges of the variables considered fall into the common practice, as given in Table 3.
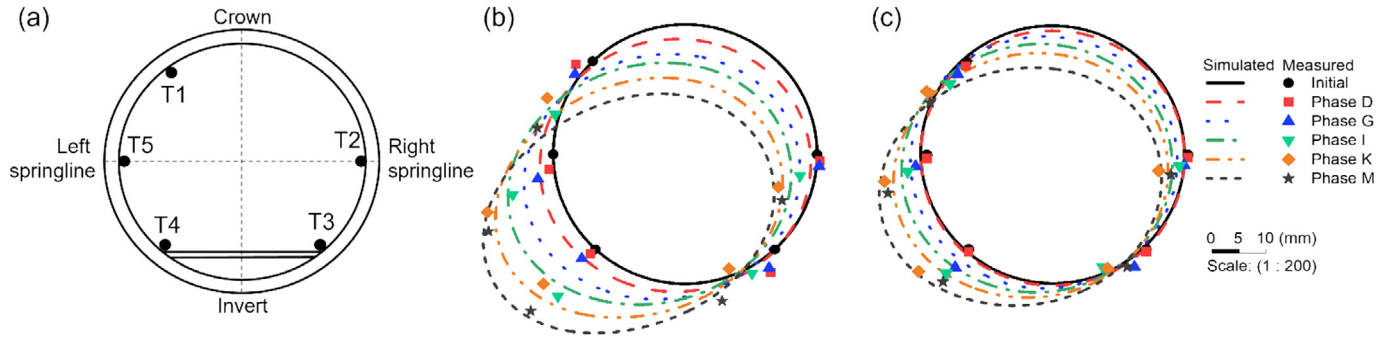
Fig. 7. Comparison of numerical results against field monitoring data for twin tunnels. (a) Layout of deformation markers, (b) displacement of UT, and (c) displacement of DT.

Table 3
Values of influential factors considered in this study.

Type	Parameter	Value
Soil properties	Combination of tangent of friction angle and normalized oedometric stiffness (tanφ', E_{oed}/σ_v')	(0.78, 446)[a], (0.57, 85)[b], (0.73, 144)[c]
Excavation size	Excavation depth, H (m)	15, 18, 21, 24
	Excavation width, B (m)	10, 20, 50
Diaphragm wall	Thickness of wall, t (m)	0.8, 1.0, 1.2
Tunnel position	Horizontal distance from retaining wall, D_h (m)	6, 9, 12, 15, 18, 21, 27, 33, 45
	Vertical distance from ground, D_v (m)	9, 12, 15, 18, 21, 24, 30, 36, 48

Note: [a]Reference from GU1; [b]Reference from GU2; [c]Reference from GU3.

It's important to note that both the friction angle and oedometric stiffness were determined by accounting for the different soil units encountered within the excavation depth: GU1 (silty sand with sandy silt), GU2 (silty clay), and GU3 (sandy silt with silty clay). Using the calibrated HSSmall constitutive model parameters and following the orthogonality principle (Table 3), a total of 8748 numerical cases are performed using an in-situ test-based finite element method (FEM) model.

5 Data-driven modelling

5.1 Machine learning algorithms

Predicting deformation responses in a deep excavation-soil-tunnel system is a complex high-dimensional nonlinear regression problem. In this case, ML algorithms are well-suited for this task due to their efficiency and strong generalization capabilities. However, each algorithm has its own advantages and drawbacks. For instance, artificial neural network (ANN) can automatically extract features and handle complex nonlinear relationships, but they require substantial training resources and are prone to overfitting. Random forest (RF) offers excellent robustness and generalization, yet struggles with high-dimensional data. Support vector machines (SVM) perform well with high-dimensional, small-sample datasets but are sensitive to hyperparameter tuning. Light gradient boosting machine (LightGBM) provides fast training but carries a higher overfitting risk. Therefore, we conducted a comprehensive comparison of these ML algorithms to identify the best-performing model for the problem studied.

5.1.1 ANN

ANN is an information processing model designed to simulate and predict complex non-linear behavior (Zhang et al., 2022). Figure 8(a) shows a typical ANN structure consisting of one input layer, one or more hidden layers, and one output layer. A set of neurons are arranged in each layer and connected through weights and bias. The input data are firstly presented through the input layer and then pass through the hidden layer(s) being processed by the neural network to eventually predict values for the output layer. This process can be expressed mathematically by considering a feedforward propagation process that the output of the i-th neuron in the k-th layer ($\tilde{y}_i^k$) can be given by assuming n neurons in the $(k–1)$-th layer:

$$\tilde{y}_i^k = f\left(\sum_{j=1}^{n} \omega_{ij}^k x_j^{k-1} + b_i^k\right), \tag{1}$$

where x_j^{k-1} is the output of the j-th neuron in the $(k–1)$-th layer; ω_{ij}^k is the weight between the two neurons of the x_j^{k-1} and $\tilde{y}_i^k$; b_i^k is the bias of the i-th neuron in the k-th layer. f represents the activation function. The training implementation of ANN can be considered into two phases: forward calculation and backward propagation.
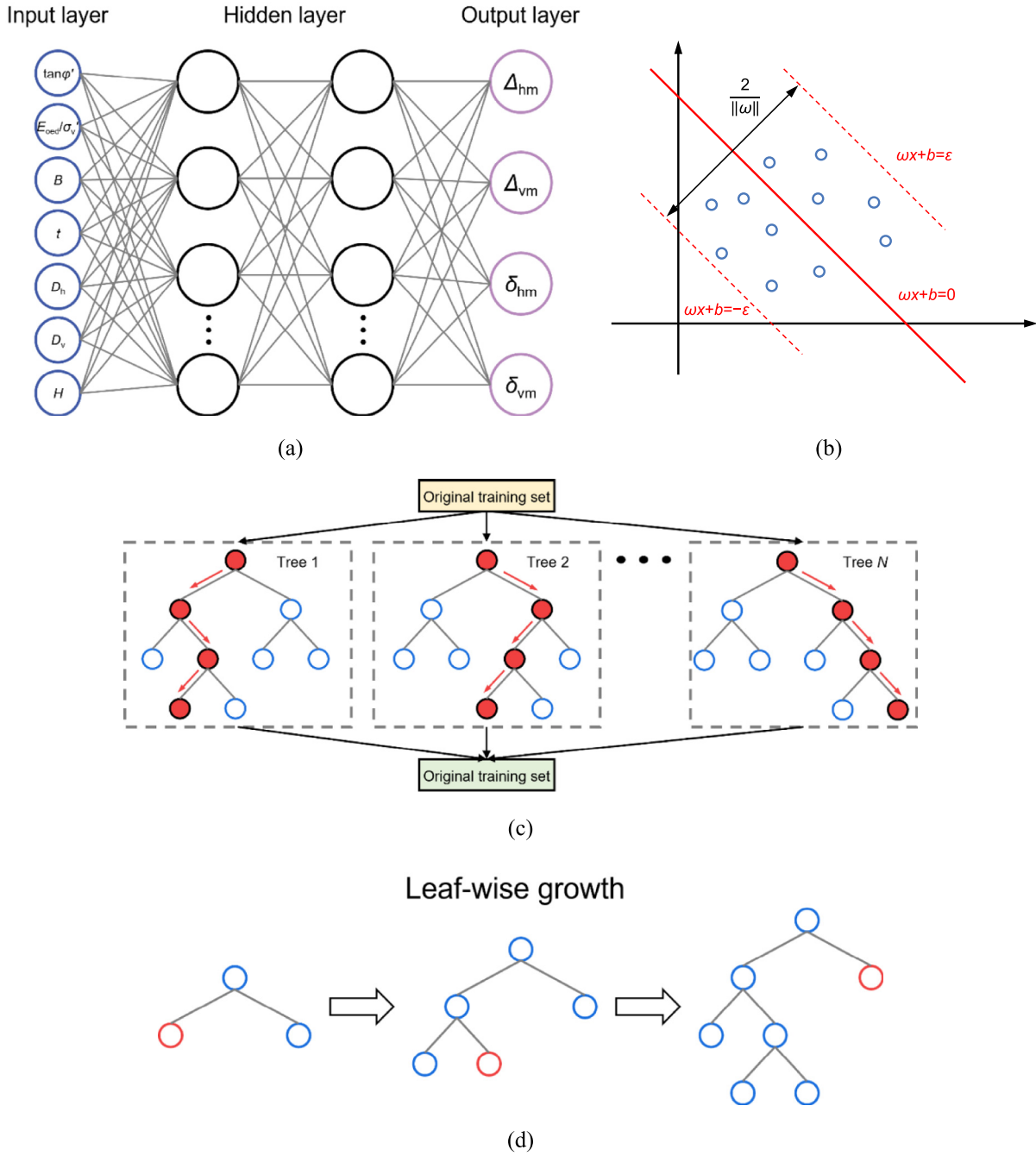
Fig. 8. Schematic diagrams of three classical ML algorithms. (a) ANN, (b) SVM, (c) RF, and (d) LightGBM.

5.1.2 SVM

Based on the concept of structural risk minimization, a SVM attempts to minimize the empirical risk and Vapnik-Chervonenkis dimension (Basak et al., 2007), as well as to find a function that satisfies the following expression:

$$\begin{cases} \min(\|\boldsymbol{\omega}\|^2/2) \\ \text{s.t.} \left| \sum_{i=1}^{M} \omega_i \phi_i(x) + b - y_i \right| \leq \varepsilon \end{cases},\tag{2}$$

where $\boldsymbol{\omega}$ is the weight vector, ω_i is the value of weight, M is the size of datasets, ϕ is the kernel function, b is the threshold, y_i is the truth value, and ε is the value of the deviation.

To better manage nonlinear regression problems and reduce computational cost, the inner product operation is often replaced by a kernel function (Mahdevari et al., 2014), so as to create a high-dimensional feature space where data can be fitted by a linear equation, as shown in Fig. 8(b). In this paper, the Gaussian function is employed, which is defined as follows:

$$\phi(x_i, x_j) = \exp\left(-\gamma \|x_i - x_j\|^2\right)(\gamma > 0),\tag{3}$$

where γ is the kernel parameter, and x_i, x_j are the input element.

5.1.3 RF

RF is an ensemble algorithm including many decision trees and bootstrap aggregation, as shown in Fig. 8(c). The bagging method and the selection of random feature attributions are considered in the RF model, which effectively avoids overfitting. Firstly, by employing the Bootstrap technique, N decision trees are generated through random sampling from the original training set. Subsequently, a portion of feature attributes is randomly chosen from all feature attributes for node splitting, constructing a single regression decision tree (P. Zhang et al., 2020). The aforementioned steps are reiterated to establish multiple regression decision trees, allowing each tree to grow to its fullest extent. Finally, the outputs of all regression decision trees are averaged to obtain the final prediction results, as shown in the following equation:

$$\tilde{y} = \frac{1}{N} \sum_{i=1}^{N} f_i(x), \tag{4}$$

where $\tilde{y}$ is the prediction output of the RF and $f_i(x)$ is the prediction output of regression decision tree.

5.1.4 LightGBM

LightGBM is another evolutionary version of gradient boosting decision tree (Ke et al., 2017). Through different optimization methods, LightGBM achieves faster training efficiency and lower memory usage. Aiming at the generative process of the decision tree, LightGBM adopts 'leaf-wise tree growth' algorithm, as shown in Fig. 8(d). It will choose the leaf with the maximum delta loss for growing, thereby guaranteeing the efficiency of the algorithm. Furthermore, LightGBM uses a histogram algorithm to find splitting points, and can directly manage category characteristics. These advantages make LightGBM popular for processing large-scale data.

5.2 Data processing

The input and output features have been discussed previously, and summarized in Table 3. For all the related horizontal displacement, the negative value represents a movement towards deep excavations while the positive represents a movement away from deep excavations. Similarly, for the vertical displacement, the negative value represents downward movement while the positive represents upward movement.

For the total of 8748 groups of data, the random 80% of total data are used as the training dataset, while the remaining 20% of data is used as the testing dataset for verifying the generalization ability of developed ML algorithms (P. Zhang et al., 2020). To ensure consistent scaling and improve model performance, all input features were normalized to a 0–1 range using the following equation:

$$x_{\text{norm}} = \frac{x - x_{\min}}{x_{\max} - x_{\min}}, \tag{5}$$

where x is the raw input variables before normalization, x_{norm} is the input variables after normalization, $x_{\min}$ and $x_{\max}$ are the minimum and maximum values of the input variables, respectively.

5.3 Construction of ML algorithms

To optimize the performance of the ML algorithms, key hyperparameters for ANN, SVM, RF, and LightGBM were fine-tuned using a trial-and-error approach. For ANN, we first defined reasonable parameter ranges: 1–4 hidden layers, 10–50 neurons per layer, and a learning rate between 0.0001 and 0.01. A grid search was conducted to identify promising hyperparameter combinations, followed by manual refinement to improve performance on both training and testing sets. A similar process was applied to RF, SVM, and LightGBM, with the final tuned hyperparameters listed in Table 4.

The ANN was trained using the Levenberg-Marquardt algorithm for weight and bias optimization, with Tanh as the activation function for hidden layers. To prevent overfitting, L2 regularization was added to the loss function, and early stopping was implemented—halting training if the test loss increased for six consecutive epochs. For SVM, we selected a Gaussian kernel with an automatically tuned γ parameter. In RF, the model used 40 decision trees, each with a maximum of 2 leaves per tree. Additionally, the boosting learning rate was set to a small value of 0.06 to ensure a super stability of LightGBM. Other unspecified hyperparameters left at their default values. To ensure robustness, we repeated each training process five times with different random seeds and reported the average results.

The model fitting performance is quantified by the coefficient of determination (R^2) in Eq. (6). Besides, the prediction errors between prediction and target values are measured by the mean absolute percentage error (MAPE) using Eq. (7), the root mean square error (RMSE) in Eq. (8), and the mean absolute error (MAE) in Eq. (9). Additionally, the relative error (RE) (shown in Eq. (10)) is further used to visualize the error distribution among predicted results.

$$R^2 = 1 - \frac{\sum_{i=1}^{M}\left(y_i - \tilde{y}_i\right)^2}{\sum_{i=1}^{M}\left(y_i - \bar{y}\right)^2}, \tag{6}$$

$$\text{MAPE} = \frac{1}{M} \sum_{i=1}^{M} \left| \frac{\tilde{y}_i - y_i}{y_i} \right| \times 100\%, \tag{7}$$

$$\text{RMSE} = \sqrt{\frac{1}{M} \sum_{i=1}^{M} \left(\tilde{y}_i - y_i\right)^2}, \tag{8}$$

$$\text{MAE} = \frac{1}{M} \sum_{i=1}^{M} \left| \tilde{y}_i - y_i \right|, \tag{9}$$

Table 4
Hyperparameters of ML algorithms.

ML algorithm	Hyperparameters	Value
ANN	Number of hidden layers	2
	Number of neurons	[20, 10]
	Initial learning rate	0.001
SVM	Kernel function	Gaussian
	Kernel parameter γ	Auto
RF	Number of decision trees	40
	Leaf in each tree	2
LightGBM	Maximum tree depth for base learners	5
	Boosting learning rate	0.06
	Number of boosted trees to fit	500

$$RE = |\frac{\tilde{y}_i - y_i}{y_i}|, \qquad (10)$$

where $\tilde{y}_i$ and y_i denote the predicted and true values of a neural network, respectively; $\bar{y}$ is the mean true value.

### 5.4 Results of data-driven models

Figure 9 presents the performance evaluation of three machine learning algorithms across all output variables. The four models all demonstrate robust training performance without overfitting, achieving R^2 values exceeding 93.8% on both training and testing datasets. Among them, the ANN performs best as it has the highest fitting degree (R^2) and the lowest error (MAPE, MAE, RMSE) for four
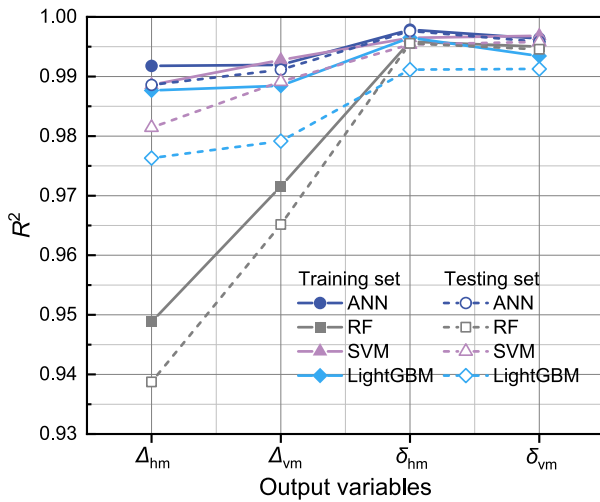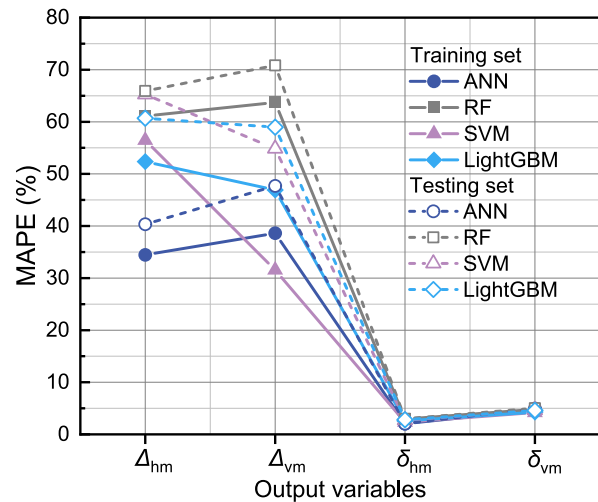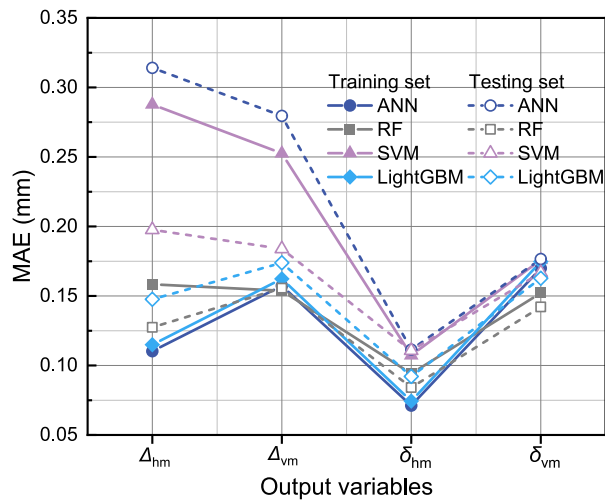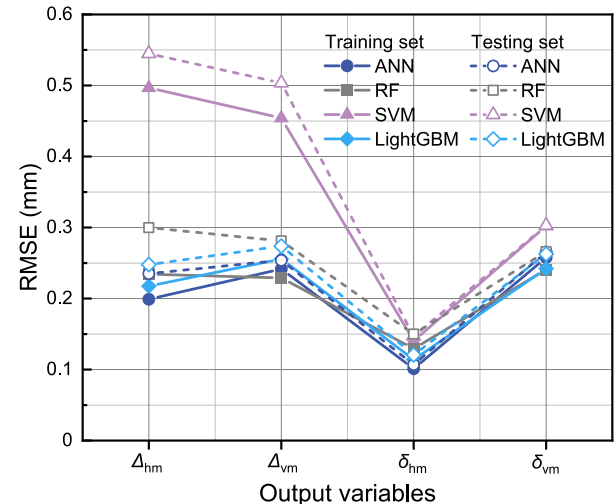
Fig. 9. Comparison of different ML algorithms in evaluation indexes of (a) R^2, (b) MAPE, (c) MAE, and (d) RMSE for each output variable.

outputs in the testing set, followed by the LightGBM, RF and SVM in descending order of performance.

Among the output variables, the model achieves the most accurate predictions for maximum wall deflection (δ_{hm}), showing the highest R^2 and lowest MAPE, MAE, and RMSE values. Maximum ground surface settlement (δ_{vm}) demonstrates slightly lower but still strong predictive performance. While tunnel displacements (Δ_{hm} and Δ_{vm}) prove somewhat more challenging to predict accurately, the ANN model maintains exceptional performance with R^2 values above 99% for both horizontal and vertical tunnel displacements in training and testing sets, significantly outperforming both RF and SVM alternatives.

Figure 10 presents a comparative visualization of predicted versus actual values for all four output variables in the testing set, with the 45° line representing perfect prediction. The scatter plots reveal distinct performance patterns among the models: while SVM predictions show considerable dispersion, ANN results cluster tightly around the reference line, demonstrating superior predictive accuracy. This visual analysis confirms ANN's outstanding performance relative to other models, though minor deviations from true values remain observable across all predictions. The persistent discrepancies between predicted and measured values can be attributed to fundamental limitations in machine learning modeling. Even high-performing
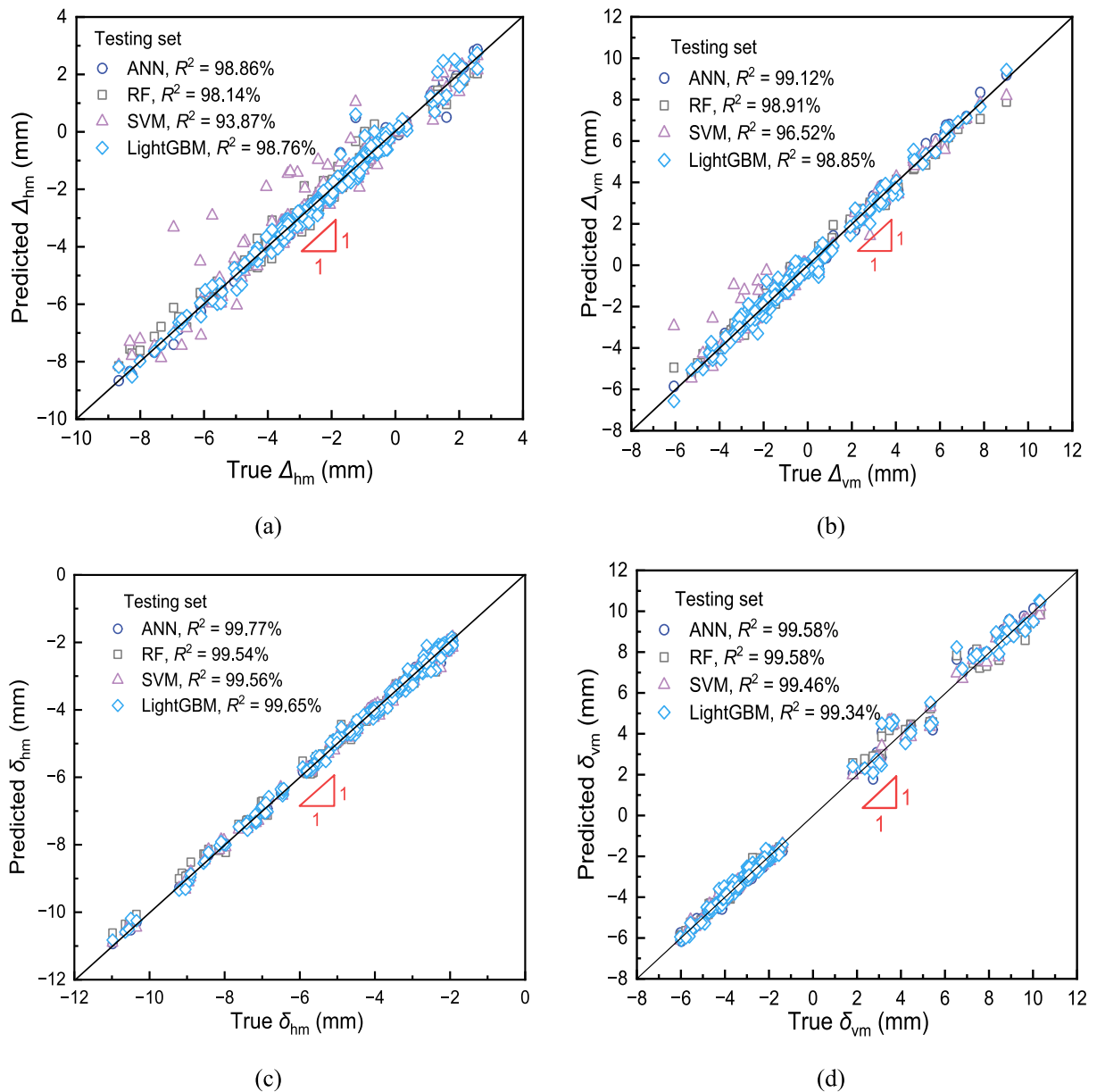

Fig. 10. Analysis of predicted output variables with true values in the testing set for (a) the maximum horizontal displacement of the tunnel, Δ_{hm}, (b) the maximum vertical displacement of the tunnel, Δ_{vm}, (c) the maximum horizontal displacement of retaining wall, δ_{hm}, and (d) the maximum ground surface settlement, δ_{vm}.

algorithms cannot achieve perfect (100%) fit due to (a) inherent model approximation capabilities; (b) potential noise in training data; and (c) the complex nonlinear nature of geotechnical systems.

Figure 11 presents the RE distributions of the four machine learning models for the testing set. The prediction errors for tunnel lining displacements (both horizontal and vertical) are marginally higher than those for wall deflection and ground surface settlement. In general, superior predictive performance is characterized by error distributions that are tightly clustered around zero with minimal spread. As shown in Fig. 11, the ANN model demonstrates the most satisfied error distribution, with errors concentrated near zero and showing significantly less dispersion compared to RF, SVM, and LightGBM. While the other models exhibit occasional larger prediction errors in extreme cases, ANN maintains consistently high accuracy, further corroborating its superior performance for the problem studied.

Figure 12 presents the SHapley Additive exPlanations (SHAP) values derived from the ANN model, revealing the relative importance of input parameters on deformation responses. The analysis demonstrates that soil properties ($\tan\varphi'$ and E_{oed}/σ_v') dominate the deformation behavior, highlighting the soil-dependent nature of excavation-induced risks. Excavation geometry (B and H) emerges as the second most influential factor that is directly relevant to the unloading effects. Tunnel position (D_h and D_v) exhibits comparatively lower importance, but that does not mean its impact on deformation response, particularly tunnel displacements, can be negligible. The wall thickness (t) shows minimal impact across all output variables, likely due to the substantial embedded depth of the retaining structures and overconservative design of wall stiffness in this study. However, parameters showing limited impact here could become crucial under different conditions—for instance, wall thickness would gain importance in excavations with shallower embedded walls.
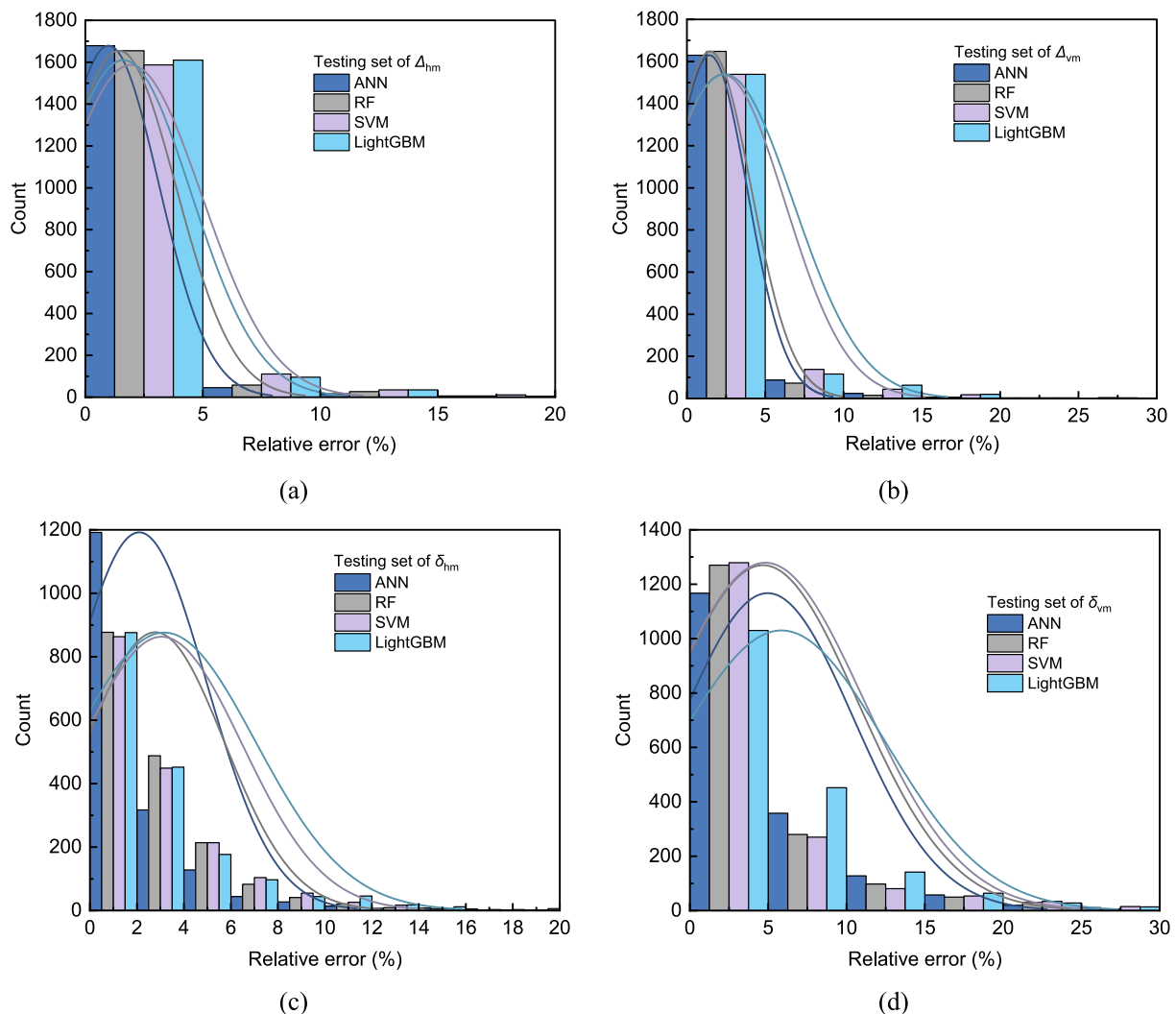

(a)

(b)

(c)

(d)

Fig. 11. Comparison of the relative error between three ML algorithms in the testing set for (a) the maximum horizontal displacement of the tunnel, $\varDelta_{hm}$, (b) the maximum vertical displacement of the tunnel, $\varDelta_{vm}$, (c) the maximum horizontal displacement of retaining wall, δ_{hm}, and (d) the maximum ground surface settlement, δ_{vm}.
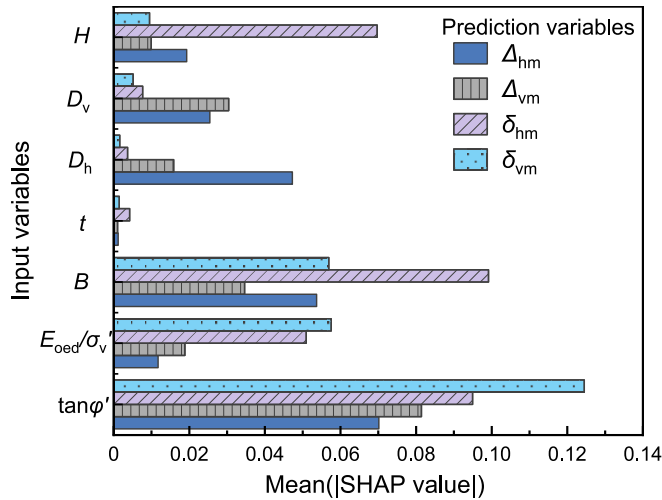
Fig. 12. Significance of input variables to each output variable.

6 Generalization in practical application

The preceding analysis has demonstrated the effectiveness of data-driven approaches for predicting deformations in deep excavations and nearby tunnels. Based on comprehensive performance evaluation, the ANN model outperforms other ML algorithms and is therefore selected for practical implementation. Table 5 examines the ANN model's generalization capability through application to ten real-world case studies of deep excavation projects near existing tunnels. The table compiles project-specific input

and output parameters obtained from the literature, along with averaged geotechnical properties derived from multiple soil strata.

Figure 13 compares the ANN model predictions with field measurements, alongside results from several empirical equations. As shown in Fig. 13(a), the ANN model achieves excellent agreement ($R^2 = 94.3\%$) with measured maximum tunnel horizontal displacements, while the empirical methods of Ding et al. (2021) and Liu et al. (2016) show significant deviations, particularly for Cases 4 and 10. Similar superior performance is observed for vertical tunnel displacements (Fig. 13(b)), where the ANN predictions align closely with measurements compared to the empirical approaches of Ding et al. (2021) and Zhuang et al. (2023). The significant deviations of empirical approaches from actual values stem from their inability to account for critical influencing factors through oversimplified fitting equations.

For the maximum wall deflection (Fig. 13(c)), the ANN model demonstrates strong predictive capability ($R^2 = 95.3\%$), whereas the empirical equations by Tan et al. (2015) and Liu et al. (2016) both underestimate the values. Likewise, in predicting ground surface settlement (Fig. 13(d)), the data-driven model outperforms empirical methods, which fail to capture the measured trends accurately.

The observed discrepancies in empirical methods stem from their simplified assumptions and inability to account for multiple complex influencing factors. Although the ANN model also exhibits minor deviations in some

Table 5
Detailed information on excavation projects from the literature.

Case No.	Case name	Input variables							Output variables (mm)			
		$\tan\varphi'$	E_{oed}/σ_v'	B (m)	H (m)	t (m)	D_h (m)	D_v (m)	Δ_{hm}	Δ_{vm}	δ_{hm}	δ_{vm}
1	A deep excavation in Shanghai, China (D. Zhang et al., 2020)	0.630	44.8	50.0	9.70	1.0	21.9	15.9	–	–	–	16.5
2	Rapid-Transit Tram rail (BRT line 1) in Nanjing, China (Zhuang et al., 2023)	0.538	195	50.0	11.50	1.0	14.0	17.5	13.5	11.8	52.0	–
3	A deep excavation in Tianjin, China (Zheng et al., 2018)	0.477	65.1	50.0	15.00	1.0	16.5	14.6	8.6	–8.6	50.0	–
4	A Taipei Rapid Transit System TRTS tunnel to adjacent excavation (Chang et al., 2001)	0.625	80.0	46.0	21.00	1.0	14.5	7.3	27.0	–33.0	53.0	–
5	Shanghai New World Commercial City Complex (Hu et al., 2003)	0.649	70.0	32.5	12.50	0.8	7.4	3.0	9.0	–5.0	28.5	23.1
6	A deep excavation adjacent to Metro Line 6 in Tianjin, China (Zheng et al., 2020b)	0.518	87.5	14.4	30.50	1.2	6.0	20.6	4.6	–2.1	20.0	–
7	A deep excavation in Shanghai, China (Liu et al., 2016)	0.532	60.0	54.0	14.90	0.8	17.6	12.3	3.0	5.0	15.0	–11.0
8	Luneng urban complex in Tianjin, China (Zheng et al., 2020a)	0.462	56.1	60.0	16.15	1.1	11.6	11.9	5.0	–	20.0	–
9	A deep excavation adjacent to Ningbo Metro Line 2 (Bian et al., 2021)	0.352	50.0	200.0	15.90	1.0	11.5	8.0	17.0	24.0	–	70.0
10	Shanghai International Air Service Center (Zhang et al., 2015)	0.414	64.0	180.0	15.70	1.0	8.3	8.4	32.5	–	60.0	–

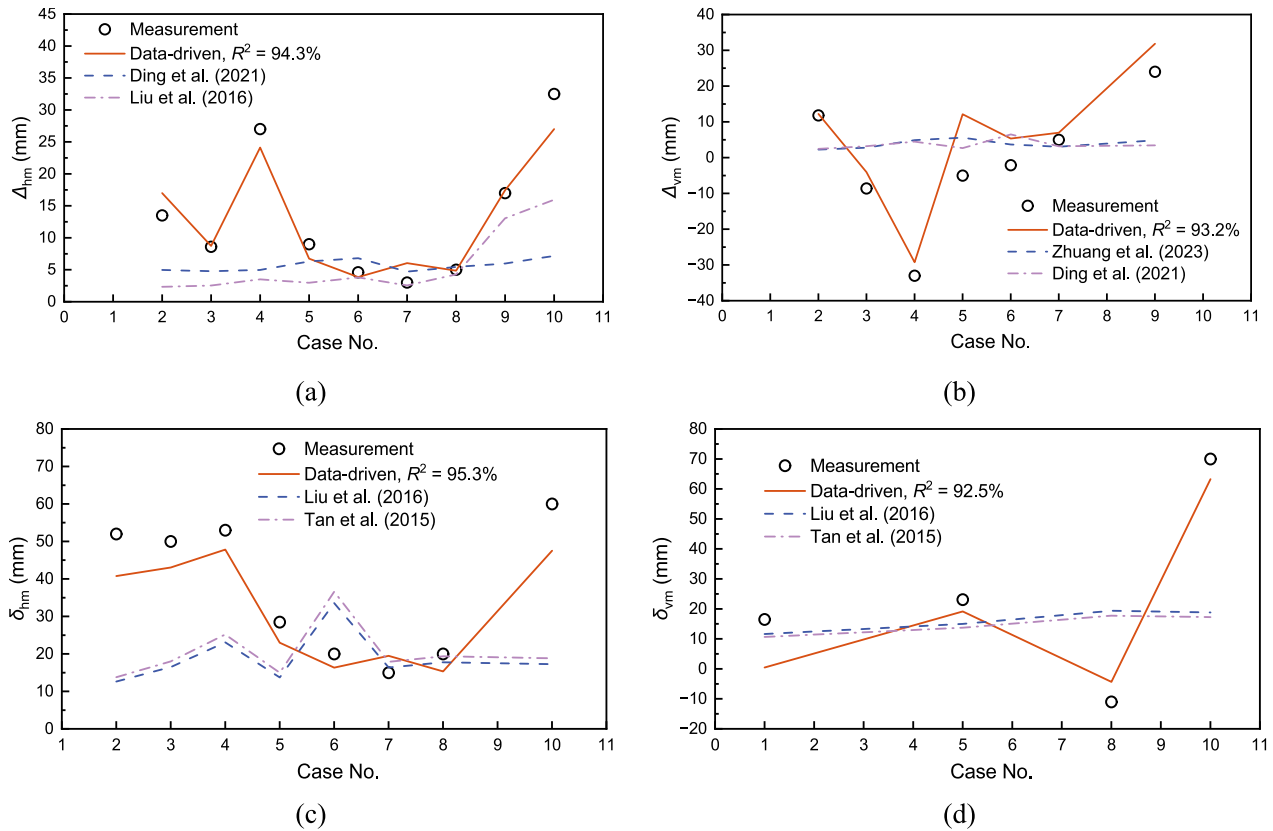Fig. 13. Comparison of the measurements and predictions by data-driven model for (a) the maximum horizontal displacement of the tunnel, Δ_{hm}, (b) the maximum vertical displacement of the tunnel, Δ_{vm}, (c) the maximum horizontal displacement of retaining wall, δ_{hm}, and (d) the maximum settlement of ground, δ_{vm}.

cases—likely due to varying construction conditions and soil stratigraphy (Table 5) beyond the training dataset—it remains a reliable tool for preliminary design and construction-phase assessments of excavation-induced deformations near existing tunnels.

The dataset employed for data-driven model training was generated entirely from an in-situ test-based FE model, instead of realistic measurements. While this approach offers the advantage of systematically isolating and quantifying the influence of key parameters—providing valuable reference for engineering practice—it inherently introduces some discrepancies when compared to actual field observations. Furthermore, since the soil parameters are the site-specific, the model's extrapolation capability and generalizability may be limited when applied to scenarios beyond the parameter ranges considered in this study.

7 Conclusions

This study has developed an integrated approach combining in-situ testing, numerical modeling, and machine learning to predict deformation responses in deep excavations adjacent to existing tunnels. Using CPT/CPTU and DMT/SDMT data, we calibrated an advanced HSSmall constitutive model, developing a unified parameter estimation method. The validated numerical model generated 8748 data points characterizing seven key input parameters

(B, H, $\tan\varphi'$, E_{oed}/σ_v', t, D_h, and D_v) and four output deformation measures (Δ_{hm}, Δ_{vm}, δ_{hm}, and δ_{vm}).

Among four optimized ML algorithms (ANN, SVM, RF, and LightGBM), ANN demonstrated superior predictive accuracy (quantified by R^2, MAPE, MAE, and RMSE metrics). Validation against ten real-world cases showed the ANN model outperformed existing empirical equations in predicting deformation responses. This integrated approach significantly enhances evaluation efficiency and accuracy, particularly valuable when geotechnical data are limited.

This study provides engineers with a practical framework for preliminary design and decision-making during deep excavations adjacent to existing tunnels in soft soils. While representing a significant advancement, future work should address: (a) parameter uncertainty arising from simplified soil stratigraphy and empirical correlations; (b) extension to more different soil types and more influencing factors (e.g., surcharge loading) to improve generalizability; (c) prediction of complete deformation profiles rather than just maximum values.

Data availability

The data that support the findings of this study are available from the corresponding author upon reasonable request.

CRediT authorship contribution statement

Declaration of competing interest

The authors declare that they have no known competing financial interests or personal relationships that could have appeared to influence the work reported in this paper.

Acknowledgement

References

ACI Committee (2008). *Building code requirements for structural concrete (ACI 318-08) and commentary*. American Concrete Institute.

Agaiby, S. S., & Mayne, P. W. (2019). CPT evaluation of yield stress profiles in soils. *Journal of Geotechnical and Geoenvironmental Engineering, 145*(12), 04019104.

Amoroso, S., Monaco, P., Lehane, B., & Marchetti, D. (2014). Examination of the potential of the seismic dilatometer (SDMT) to estimate in situ stiffness decay curves in various soil types. *Soils and Rocks, 37*(3), 177–194.

Basak, D., Pal, S., & Patranabis, D. C. (2007). Support vector regression. *Neural Information Processing-Letters and Reviews, 11*(10), 203–224.

Benz, T. (2007). *Small-strain stiffness of soils and its numerical consequences*. [Doctoral dissertation, University of Stuttgart, Germany].

Bian, X. C., Hu, H. Q., Zhao, C., Ye, J. N., & Chen, Y. M. (2021). Protective effect of partition excavations of a large-deep foundation pit on adjacent tunnels in soft soils: A case study. *Bulletin of Engineering Geology and the Environment, 80*(7), 5693–5707.

Brinkgreve, R., Kumarswamy, S., Swolfs, W., Waterman, D., Chesaru, A., & Bonnier, P. (2016). PLAXIS 2016. PLAXIS bv, the Netherlands.

Chang, C. T., Sun, C. W., Duann, S., & Hwang, R. N. (2001). Response of a Taipei Rapid Transit System (TRTS) tunnel to adjacent excavation. *Tunnelling and Underground Space Technology, 16*(3), 151–158.

Chen, R. P., Meng, F. Y., Li, Z. C., Ye, Y. H., & Ye, J. N. (2016). Investigation of response of metro tunnels due to adjacent large excavation and protective measures in soft soils. *Tunnelling and Underground Space Technology, 58*, 224–235.

Cheng, H. Z., Chen, R. P., Wu, H. N., & Meng, F. Y. (2020). A simplified method for estimating the longitudinal and circumferential behaviors of the shield-driven tunnel adjacent to a braced excavation. *Computers and Geotechnics, 123*, 103595.

Daxer, H. P., Schweiger, H., & Tschuchnigg, F. (2023). Ultimate limit state design of deep excavation problems according to EC7 using numerical methods (NUMGE 2023). In *Proceedings of the 10th European conference on numerical methods in geotechnical engineering* (pp. 1–6). London: Imperial College London.

Di Mariano, A., Amoroso, S., Arroyo, M., Monaco, P., & Gens, A. (2019). SDMT-based numerical analyses of deep excavation in soft soil. *Journal of Geotechnical and Geoenvironmental Engineering, 145*(1), 04018102.

Ding, Z., Zhang, X., Liang, F. Y., Cheng, D. J., & Wang, L. Q. (2021). Research and prospects regarding the effect of foundation pit excavation on an adjacent existing tunnel in soft soil. *China Journal of Highway and Transport, 34*(3), 50–70 (in Chinese).

Doležalová, M. (2001). Tunnel complex unloaded by a deep excavation. *Computers and Geotechnics, 28*(6–7), 469–493.

Fabris, C., Schweiger, H. F., Pulko, B., Woschitz, H., & Račanský, V. (2021). Numerical simulation of a ground anchor pullout test monitored with fiber optic sensors. *Journal of Geotechnical and Geoenvironmental Engineering, 147*(2), 04020163.

Guo, H. W., Zhuang, X. Y., Fu, X. L., Zhu, Y. Z., & Rabczuk, T. (2023). Physics-informed deep learning for three-dimensional transient heat transfer analysis of functionally graded materials. *Computational Mechanics, 72*(3), 513–524.

Hu, Z. F., Yue, Z. Q., Zhou, J., & Tham, L. G. (2003). Design and construction of a deep excavation in soft soils adjacent to the Shanghai Metro tunnels. *Canadian Geotechnical Journal, 40*(5), 933–948.

Huang, X., Schweiger, H. F., & Huang, H. W. (2013). Influence of deep excavations on nearby existing tunnels. *International Journal of Geomechanics, 13*(2), 170–180.

Ke, G. L., Meng, Q., Finley, T., Wang, T. F., Chen, W., Ma, W. D., Ye, Q. W., & Liu, T. Y. (2017). Lightgbm: A highly efficient gradient boosting decision tree. In *Proceedings of the 31st international conference on advances in neural information processing systems*. Long Beach, the United States.

Khoiri, M., & Ou, C. Y. (2013). Evaluation of deformation parameter for deep excavation in sand through case histories. *Computers and Geotechnics, 47*, 57–67.

Kung, G. T., Juang, C. H., Hsiao, E. C., & Hashash, Y. M. (2007). Simplified model for wall deflection and ground-surface settlement caused by braced excavation in clays. *Journal of Geotechnical and Geoenvironmental Engineering, 133*(6), 731–747.

Lai, F. W., Zhang, N. N., Liu, S. Y., Sun, Y. X., & Li, Y. L. (2021). Ground movements induced by installation of twin large diameter deeply-buried caissons: 3D numerical modeling. *Acta Geotechnica, 16*(9), 2933–2961.

Lai, F. W., Liu, S. Y., Li, Y. L., & Sun, Y. X. (2022). A new installation technology of large diameter deeply-buried caissons: Practical application and observed performance. *Tunnelling and Underground Space Technology, 125*, 104507.

Lai, F. W., Shiau, J., Keawsawasvong, S., Chen, F. Q., Banyong, R., & Seehavong, S. (2023). Physics-based and data-driven modeling for stability evaluation of buried structures in natural clays. *Journal of Rock Mechanics and Geotechnical Engineering, 15*(5), 1248–1262.

Lai, F. W., Tschuchnigg, F., Schweiger, H. F., Liu, S. Y., Shiau, J., & Cai, G. J. (2025). A numerical study of deep excavations adjacent to existing tunnels: Integrating CPTU and SDMT to calibrate soil constitutive model. *Canadian Geotechnical Journal, 62*, 1–23.

Lee, J., Eun, J., Lee, K., Park, Y., & Kim, M. (2008). In-situ evaluation of strength and dilatancy of sands based on CPT results. *Soils and Foundations, 48*(2), 255–265.

Li, M. G., Chen, J. J., Wang, J. H., & Zhu, Y. F. (2018). Comparative study of construction methods for deep excavations above shield tunnels. *Tunnelling and Underground Space Technology, 71*, 329–339.

Li, M. G., Xiao, X., Wang, J. H., & Chen, J. J. (2019). Numerical study on responses of an existing metro line to staged deep excavations. *Tunnelling and Underground Space Technology, 85*, 268–281.

Liang, R. Z., Wu, W. B., Yu, F., Jiang, G. S., & Liu, J. W. (2018). Simplified method for evaluating shield tunnel deformation due to adjacent excavation. *Tunnelling and Underground Space Technology, 71*, 94–105.

Liao, S. M., Wei, S. F., & Shen, S. L. (2016). Structural responses of existing metro stations to adjacent deep excavations in Suzhou, China. *Journal of Performance of Constructed Facilities, 30*(4), 04015089.

Liu, B., Zhang, D. W., Yang, C., & Zhang, Q. B. (2020). Long-term performance of metro tunnels induced by adjacent large deep excavation and protective measures in Nanjing silty clay. *Tunnelling and Underground Space Technology, 95*, 103147.

Liu, B., Wu, W. W., Lu, H. P., Chen, S., & Zhang, D. W. (2024a). Effect and control of foundation pit excavation on existing tunnels: A state-of-the-art review. *Tunnelling and Underground Space Technology, 147*, 105704.

Liu, G. B., Huang, P., Shi, J. W., & Ng, C. W. W. (2016). Performance of a deep excavation and its effect on adjacent tunnels in shanghai soft clay. *Journal of Performance of Constructed Facilities, 30*(6), 04016041.

Liu, M. P., Sun, E. C., Zhang, N. N., Lai, F. W., & Fuentes, R. (2024b). A virtual calibration chamber for cone penetration test based on deep-learning approaches. *Journal of Rock Mechanics and Geotechnical Engineering, 16*(12), 5179–5192.

Liu, M. P., Zhuang, P. Z., & Lai, F. W. (2024c). A Bayesian optimization-genetic algorithm-based approach for automatic parameter calibration of soil models: Application to clay and sand model. *Computers and Geotechnics, 176*, 106717.

Lu, T. S., Liu, S. Y., Wu, K., Cai, G. J., & Li, Z. (2023a). Semi-analytical approach for the load-settlement response of a pile considering excavation effects. *Acta Geotechnica, 18*(3), 1179–1197.

Lu, T. S., Wu, K., Liu, S. Y., & Cai, G. J. (2023b). Method for estimating three-dimensional effects on braced excavation in clay. *Tunnelling and Underground Space Technology, 141*, 105355.

Lunne, T., Powell, J. J. M., & Robertson, P. K. (2002). *Cone penetration testing in geotechnical practice*. CRC Press.

Mahdevari, S., Shahriar, K., Yagiz, S., & Shirazi, M. A. (2014). A support vector regression model for predicting tunnel boring machine penetration rates. *International Journal of Rock Mechanics and Mining Sciences, 72*, 214–229.

Marchetti, S. (1980). In situ tests by flat dilatometer. *Journal of the Geotechnical Engineering Division, 106*(3), 299–321.

Marzouk, I., Brinkgreve, R., Lengkeek, A., & Tschuchnigg, F. (2024). APD: An automated parameter determination system based on in-situ tests. *Computers and Geotechnics, 176*, 106799.

Mayne, P. W. (2005). Integrated ground behavior: In-situ and lab tests. In *Deformation characteristics of geomaterials* (pp. 155–177). CRC Press.

Mayne, P. W. (2016). Evaluating effective stress parameters and undrained shear strengths of soft-firm clays from CPT and DMT. *Australian Geomechanics Journal, 51*(4), 27–55.

Mayne, P. W., & Kulhawy, F. H. (1982). K_o-OCR relationships in soil. *Journal of the Geotechnical Engineering Division, 108*(6), 851–872.

Mayne, P. W. (2007). *Synthesisi on Cone penetration testing* NCHRP Report. Washington. D. C, the USA: Transportation Research Board.

Meng, F. Y., Chen, R. P., Wu, H. N., Xie, S. W., & Liu, Y. (2020). Observed behaviors of a long and deep excavation and collinear underlying tunnels in Shenzhen granite residual soil. *Tunnelling and Underground Space Technology, 103*, 103504.

Meng, F. Y., Chen, R. P., Xu, Y., Wu, K., Wu, H. N., & Liu, Y. (2022). Contributions to responses of existing tunnel subjected to nearby excavation: A review. *Tunnelling and Underground Space Technology, 119*, 104195.

Meng, F. Y., Chen, R. P., Xu, Y., Wu, H. N., & Li, Z. C. (2021). Centrifuge modeling of effectiveness of protective measures on existing tunnel subjected to nearby excavation. *Tunnelling and Underground Space Technology, 112*, 103880.

Meng, F. Y., Hu, B., Chen, R. P., Cheng, H. Z., & Wu, H. N. (2025). Characteristics of deformation and defect of shield tunnel in coastal structured soil in China. *Underground Space, 21*, 131–148.

Mishra, A., Anitescu, C., Budarapu, P. R., Natarajan, S., Vundavilli, P. R., & Rabczuk, T. (2024). An artificial neural network based deep collocation method for the solution of transient linear and nonlinear partial differential equations. *Frontiers of Structural and Civil Engineering, 18*(8), 1296–1310.

Ou, C. Y. (2006). *Deep excavation: Theory and practice*. CRC Press.

Robertson, P. K. (2010). Estimating in-situ soil permeability from CPT & CPTu. In *Proceedings of the 2nd international symposium on cone penetration testing*. Huntington Beach, CA, USA.

Robertson, P. K., & Cabal, K. (2010). Estimating soil unit weight from CPT. In *Proceedings of the 2nd international symposium on cone penetration testing*. Huntington Beach, CA, USA.

Robertson, P. K. (2016). Cone penetration test (CPT)-based soil behaviour type (SBT) classification system—an update. *Canadian Geotechnical Journal, 53*(12), 1910–1927.

Samaniego, E., Anitescu, C., Goswami, S., Nguyen-Thanh, V. M., Guo, H., Hamdia, K., Zhuang, X., & Rabczuk, T. (2020). An energy approach to the solution of partial differential equations in computational mechanics via machine learning: Concepts, implementation and applications. *Computer Methods in Applied Mechanics and Engineering, 362*, 112790.

Schanz, T., Vermeer, P. A., & Bonnier, P. G. (1999). The hardening soil model: Formulation and verification. In *Beyond 2000 in computational geotechnics* (pp. 281–296). London: Routledge.

Schmüdderich, C., Shahrabi, M. M., Taiebat, M., & Lavasan, A. A. (2020). Strategies for numerical simulation of cast-in-place piles under axial loading. *Computers and Geotechnics, 125*, 103656.

Schweiger, H. F. (2014). Influence of EC7 design approaches on the design of deep excavations with FEM. *Geotechnik, 37*(3), 169–176.

Shi, J. W., Ng, C. W. W., & Chen, Y. H. (2015). Three-dimensional numerical parametric study of the influence of basement excavation on existing tunnel. *Computers and Geotechnics, 63*, 146–158.

Singh, S., & Budarapu, P. R. (2024). Deep machine learning approaches for battery health monitoring. *Energy, 300*, 131540.

Siruvuri, S. D. V. S. S. V., Budarapu, P. R., & Paggi, M. (2023). Influence of cracks on fracture strength and electric power losses in Silicon solar cells at high temperatures: Deep machine learning and molecular dynamics approach. *Applied Physics A, 129*(6), 408.

Tan, Y., Li, X., Kang, Z. J., Liu, J. X., & Zhu, Y. B. (2015). Zoned excavation of an oversized pit close to an existing metro line in stiff clay: Case study. *Journal of Performance of Constructed Facilities, 29*(6), 04014158.

Van Berkom, I. E., Brinkgreve, R. B. J., De Jong, A. K., & Lengkeek, H. J. (2022). An automated system to determine constitutive model parameters from in situ tests. In *Proceedings of the 20th international conference on soil mechanics and geotechnical engineering* (ICSMGE). Sydney, Australia.

Varma Siruvuri, S. D. V. S. S., Verma, H., Javvaji, B., & Budarapu, P. R. (2022). Fracture strength of Graphene at high temperatures: Data driven investigations supported by MD and analytical approaches. *International Journal of Mechanics and Materials in Design, 18*(4), 743–767.

Wei, G., Feng, F. F., Huang, S. Y., Xu, T. B., Zhu, J. X., Wang, X., & Zhu, C. W. (2025). Full-scale loading test for shield tunnel segments: Load-bearing performance and failure patterns of lining structures. *Underground Space, 20*, 197–217.

Xu, J. M., Gao, M., Wang, Y. K., Yu, Z. H., Zhao, J. Y., & DeJong, M. J. (2025). Numerical investigation of the effects of separated footings on tunnel-soil-structure interaction. *Journal of Geotechnical and Geoenvironmental Engineering, 151*(7), 04025057.

Zhang, H.-B, Chen, J.-J, Fan, F., & Wang, J.-H. (2015). Deformation monitoring and performance analysis on the shield tunnel influenced by adjacent deep excavations. *Journal of Aerospace Engineering, 30*(2), B4015002.

Zhang, D. M., Xie, X. C., Li, Z. L., & Zhang, J. (2020a). Simplified analysis method for predicting the influence of deep excavation on existing tunnels. *Computers and Geotechnics, 121*, 103477.

Zhang, D. M., Shen, Y. M., Huang, Z. K., & Xie, X. C. (2022). Auto machine learning-based modelling and prediction of excavation-induced tunnel displacement. *Journal of Rock Mechanics and Geotechnical Engineering, 14*(4), 1100–1114.

Zhang, J. F., Chen, J. J., Wang, J. H., & Zhu, Y. F. (2013). Prediction of tunnel displacement induced by adjacent excavation in soft soil. *Tunnelling and Underground Space Technology, 36*, 24–33.

Zhang, P., Wu, H. N., Chen, R. P., Dai, T., Meng, F. Y., & Wang, H. B. (2020b). A critical evaluation of machine learning and deep learning in shield-ground interaction prediction. *Tunnelling and Underground Space Technology, 106*, 103593.

Zheng, G., Yang, X. Y., Zhou, H. Z., Du, Y. M., Sun, J. Y., & Yu, X. X. (2018). A simplified prediction method for evaluating tunnel displacement induced by laterally adjacent excavations. *Computers and Geotechnics, 95*, 119–128.

Zheng, G., He, X. P., Zhou, H. Z., Yang, X. Y., Yu, X. X., & Zhao, J. P. (2020a). Prediction of the tunnel displacement induced by laterally adjacent excavations using multivariate adaptive regression splines. *Acta Geotechnica, 15*, 2227–2237.

Zheng, G., Pan, J., Li, Y. L., Cheng, X. S., Tan, F. L., Du, Y. M., & Li, X. H. (2020b). Deformation and protection of existing tunnels at an oblique intersection angle to an excavation. *International Journal of Geomechanics, 20*(8), 05020004.

Zhuang, X. Y., Guo, H. W., Alajlan, N., Zhu, H. H., & Rabczuk, T. (2021). Deep autoencoder based energy method for the bending, vibration, and buckling analysis of Kirchhoff plates with transfer learning. *European Journal of Mechanics - A/Solids, 87*, 104225.

Zhuang, Y., Cui, X. Y., & Hu, S. L. (2023). Numerical simulation and simplified analytical method to evaluate the displacement of adjacent tunnels caused by excavation. *Tunnelling and Underground Space Technology, 132*, 104879.